ASTROBIOLOGY
Volume 18, Number 8, 2018

DOI: 10.1089/ast.2017.1780

Chemical and Optical Identification of Micrometer-Sized 1.9 Billion-Year-Old Fossils by Combining a Miniature Laser Ablation Ionization Mass Spectrometry System with an Optical Microscope

Reto Wiesendanger,[1,2] David Wacey,[3] Marek Tulej,[1] Anna Neubeck,[4] Magnus Ivarsson,[5,6] Valentine Grimaudo,[7] Pavel Moreno-García,[7] Alena Cedeño-López,[7] Andreas Riedo,[8] and Peter Wurz[1]

Abstract

The recognition of biosignatures on planetary bodies requires the analysis of the putative microfossil with a set of complementary analytical techniques. This includes localized elemental and isotopic analysis of both the putative microfossil and its surrounding host matrix. If the analysis can be performed with spatial resolution at the micrometer level and part-per-million detection sensitivities, valuable information on the (bio)chemical and physical processes that influenced the sample material can be gained. Our miniaturized laser ablation ionization mass spectrometry (LIMS)-time-of-flight mass spectrometer instrument is a valid candidate for performing the required chemical analysis *in situ*. However, up until now it was limited by the spatial accuracy of the sampling. In this contribution, we introduce a newly developed microscope system with micrometer accuracy for ultra high vacuum application, which allows a significant increase in the measurement capabilities of our miniature LIMS system. The new enhancement allows identification and efficient and accurate sampling of features of micrometer-sized fossils in a host matrix. The performance of our system is demonstrated by the identification and chemical analysis of signatures of micrometer-sized fossil structures in the 1.9 billion-year-old Gunflint chert. Key Words: Biosignatures—Gunflint chert—*In situ* mass spectrometry—Life-detection—Microscopy—Space instrumentation. Astrobiology 18, 1071–1080.

1. Introduction

In situ detection of biosignatures of extinct life on planetary bodies is a challenging endeavor because no single, unique, and easy-to-measure criterion for the presence of extinct life exists. It is rather a combination of a multitude of factors indicative that a given region was able to host life and that a putative fossil is of biological origin. Several authors have proposed multicriteria approaches for the confirmation (or rejection) of the hypothesis that a selected sample is of biological origin (Thomas *et al.*, 2004; Hofmann, 2008; Brasier and Wacey, 2012; Vago *et al.*, 2017). All studies emphasize the importance of the combination of morphological as well as sensitive chemical analysis of the putative fossil and its host at different scales (Hanauske *et al.*, 1987; Tulej *et al.*, 2014, 2015). Such analysis has the potential to detect traces of cell structures and metabolic processes of species fossilized millions to billions of years ago (Westall *et al.*, 2001; Chela-Flores and Kumar, 2008; Chela-Flores and Seckbach, 2011; Summons *et al.*, 2011; Wacey *et al.*, 2011; Chela-Flores *et al.*, 2015).

Microorganisms, including bacteria, archaea, and eukaryotes, can be found as single entities, but more often aggregate to micrometer-sized colonies that need to be identified and distinguished from their host and other impurities and inclusions for further chemical investigation. Their analysis includes the determination of isotope ratios and fractionation of biorelevant stable elements such as C, H, N, S, Fe, and Ni (Monster *et al.*, 1979; Ohmoto *et al.*, 1993; Beard *et al.*, 1999; Shen *et al.*, 2001; Ono, 2008;

[1]Space Research and Planetary Sciences, Physics Institute, University of Bern, Bern, Switzerland.
[2]Microsystems for Space Technologies Laboratory, Ecole Polytechnique Fédérale, Lausanne, Neuchâtel, Switzerland
[3]Centre for Microscopy Characterisation and Analysis, The University of Western Australia, Perth, Australia.
[4]Department of Geological Sciences, Stockholm University, Stockholm, Sweden.
[5]Department of Paleobiology, Nordic Centre for Earth Evolution, Swedish Museum of Natural History, Stockholm, Sweden.
[6]Department of Biology, University of Southern Denmark, Odense, Denmark.
[7]Department of Chemistry and Biochemistry, Interfacial Electrochemistry Group, University of Bern, Bern, Switzerland.
[8]Sackler Laboratory for Astrophysics, Leiden Observatory, Leiden University, The Netherlands.

Cameron *et al.*, 2009; Vago *et al.*, 2017). Redfield (1934) and more recently Managadze *et al.*, (2017) and Marshall (2017) also proposed the detection of elements and analysis of their ratios for the identification of biosignatures.

The microorganisms conserved in the 1.9 billion-year-old Gunflint chert serve as a Mars analogue in our study. With reference to this sample, we introduce our recently developed optical microscope that serves as a complement to the already existing, highly sensitive miniature flight prototype of a laser ablation mass spectrometer. Together, these two instruments form an instrument suite capable of performing the required chemical and optical analysis.

2. Current State-of-the-Art of Miniature Laser Ablation Ionization Mass Spectrometry Instruments and Rationale for a Microscope

In recent years, laser ablation ionization mass spectrometry (LIMS) has been proven to be a successful measurement technique for quantitative mapping of chemical composition of solid samples with high spatial resolution (Grimaudo *et al.*, 2017) down to the nanometer level (Kuznetsov *et al.*, 2015). However, this could only be achieved with the effort of many groups contributing to this field (Brinckerhoff *et al.*, 2000; Huang *et al.*, 2010; Cui *et al.*, 2012; Riedo *et al.*, 2013b, 2013c; Zhang *et al.*, 2013; Kuznetsov *et al.*, 2015).

Our miniature (ø60 mm, l = 160 mm) laser ablation ionization time-of-flight mass spectrometer (LA-TOF-MS) designed and built at the University of Bern was originally developed for *in situ* elemental and isotope analysis of solids on planetary bodies (Rohner *et al.*, 2003). A detailed description of the working principle of the instrument can be found in the studies of Riedo *et al.* (2013a, 2013c, 2017). Only a brief description is given here. The right side of Figure 1 depicts the LIMS-TOF-MS part of the instrument suite. The sample is positioned a fraction of a millimeter away from the entrance aperture of the mass spectrometer using a xyz translation stage with $100 \times 50 \times 50$ mm travel range. An ultrashort laser pulse ($\lambda = 775$ nm, ~ 180 fs, 1 kHz repetition rate, intensity ≤ 1 mJ/pulse) is sent to the instrument through optical path 1 (OP1) and focused on the sample with a lens placed at the back of the mass spectrometer. The positive ions created during the ablation process are accelerated and focused into the instrument through a series of dedicated electrodes. A reflectron type ion mirror focuses the ion beam onto a highly sensitive four-channel MCP detector with a dynamic range of up to 10^8 (Riedo *et al.*, 2017). The signal is acquired with a dedicated PC using two high speed ADC cards (8 bit, 2 channels each, with a sampling rate of up to 4 GS/s).

With the experience gained over more than a decade by investigating a wide series of samples, spanning different scientific fields ranging from astrobiology (Tulej *et al.*, 2015) to the semiconductor industry (Moreno-Garcia *et al.*, 2016), the measurement capabilities and performance parameters of the instrument have been continuously improved. Today, the system allows the study of heterogeneous materials with a depth resolution in the nanometer range, lateral resolutions of about 15–20 μm (Neuland *et al.*, 2014; Grimaudo *et al.*, 2015, 2017; Riedo *et al.*, 2015), with a sensitivity down to sub-ppm level (Riedo *et al.*, 2013a, 2013b; Riedo *et al.*, 2013c; Wiesendanger *et al.*, 2017). In these previous measurement campaigns, we performed sampling of large rectangular areas (sometimes several hundred spots) with a pitch between sampling locations close to the ablation spot diameter. This approach, later on called "rastering," is a useful technique for obtaining two-dimensional and three-dimensional (3D) chemical maps (Neuland *et al.*, 2014; Grimaudo *et al.*, 2017). However, during our previous work, it became clear that this method is too time consuming and inefficient when sampling of micrometer-sized fossils is required (Tulej *et al.*, 2015).

Figure 2 illustrates the reasons why a microscope is a mandatory complement to the LIMS-TOF-MS, which

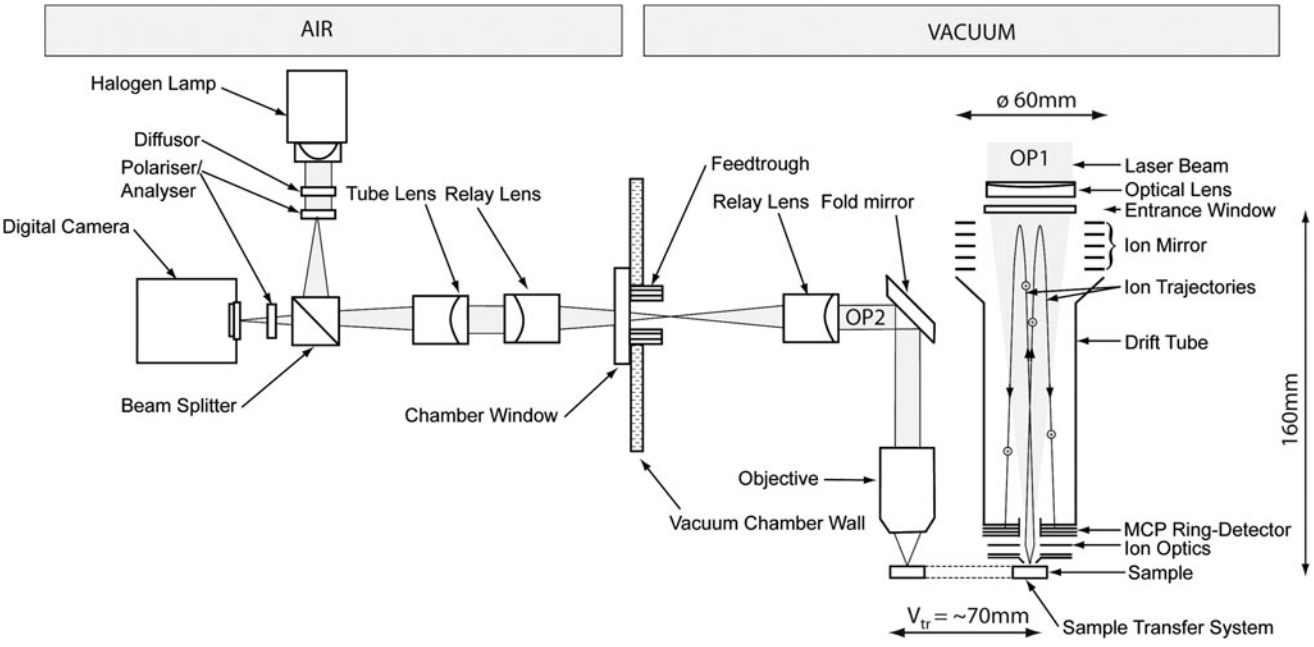

FIG. 1. Drawing of the ultra high vacuum-compatible microscope that was recently added to our miniature laser ablation ionization mass spectrometry system. Details can be found in the text. OP1, optical path 1; OP2, optical path 2.

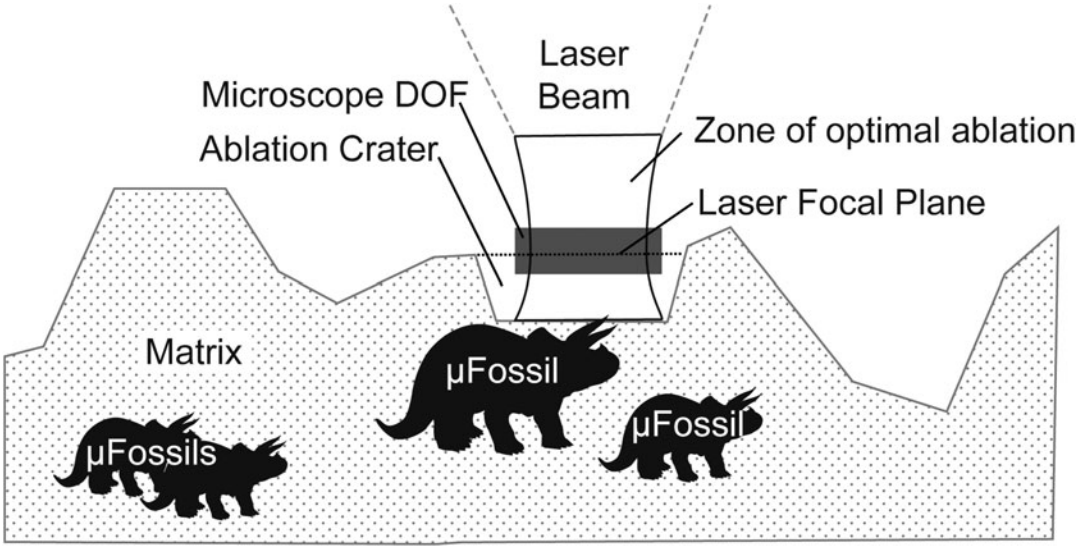

FIG. 2. Schematic representation of a sample with an uneven surface structure and containing microfossils inside a transparent matrix. DOF, depth of focus.

enables the localization of putative microfossils and the acquisition of their mass spectra at the highest possible quality. The fossils are often embedded in a matrix, with dimensions close to, or below, the ablation laser spot diameter and with a possibly irregular distribution and shape. To minimize chemical contributions from the surrounding matrix to the acquired mass spectrum from the fossil, precise targeting of the object of interest is required. This can only be achieved with a precise visual feedback of the sampled region.

Extensive sample preparation, such as polishing or thin section preparation before the mass spectrometric analysis on board of a lander or rover, is not likely to be possible, and hence samples investigated on planetary surfaces are likely to exhibit an uneven surface. The height inhomogeneities can easily be >100 µm and thereby depart from the region of optimal laser ablation. In the case of our instrument, this optimal region is $\sim\pm 50$ µm above or below the laser focus. A precise compensation of the uneven surface with the sample translation stage is, therefore, highly desirable for optimal spectral quality and comparability between different locations on the sample. A microscope system with a sufficiently small depth of focus (DOF) would permit the creation of a 3D profile of the sample surface. Calibrating the focus of the microscope to the focal point of the ablation laser would then enable the sample surface to be precisely positioned in the laser focus at any time.

Using the microscope for an optical feedback would also allow the control of the ablation process and the determination of the optimal ablation parameters for different materials, especially the laser fluence that has a major impact on the quality of the mass spectrum.

3. Microscope System

Different research groups and commercial TOF-MS manufacturers have already implemented microscopes in their instruments (Heinen *et al.*, 1983; Guest, 1984; Ma *et al.*, 1995; Zonnevylle *et al.*, 2013; Hornung *et al.*, 2014; Tulej *et al.*, 2014), and several microscopes and close up imagers were built and flown to Mars. These instruments have a resolving power between 122 and ~ 3 µm. However, a resolution of ~ 1 µm is desirable to resolve individual microbial cells (Thomas *et al.*, 2004; Hofmann, 2008; Vago *et al.*, 2017).

In the case of the LMS Instrument, direct visualization of the sample during the ablation process could be realized by using the optical path of the laser also for the microscope (OP1 on Fig. 1). However, this optical path does not offer enough numerical aperture (NA) to see the sample with 1 µm resolution. Therefore, we developed and built a solution with a secondary optical path (OP2 on Fig. 1), in which the microscope optical axis is placed parallel and offset by ~ 70 mm to the instrument axis. Using this configuration, (shown in Fig. 1), we were able to place a Nikon infinity corrected bright field microscope objective with an NA of 0.3 next to the mass spectrometer. This objective has a resolving power of 1 µm, which is sufficient to clearly resolve our ablation spots and the microbial fossils. The DOF is ~ 3 µm, which allows us to place the sample in the zone of optimal laser ablation as shown in Figure 2.

The image is focused onto an image sensor of a camera with a readily available Nikon 200 mm tube lens. Both the objective and the tube lens were disassembled and modified in-house to improve their vacuum compatibility. For ease of use, the image should be situated outside the vacuum chamber, so that the camera can be placed and operated in air. This is achieved by placing a fold mirror to transport the image through a window on a lateral side of the vacuum chamber. A relay lens system consisting of two additional Nikon 200 mm tube lenses transports the image far enough from the chamber wall to allow the installation of the camera (Allied Vision, Manta G201 with 1624×1234 pixel resolution) and the illumination system. The two relay lenses are placed on axially adjustable mounts so they can be focused to the intermediate image and the focal plane. The objective is mounted on an in-house made adjustable holder that allows the operator to shift its working plane and to align this plane with the axis of the mass analyzer.

The illumination of the sample is provided by a diffused image of a tungsten–halogen lamp that is coupled into the optical path using a broadband beam splitter (Thorlabs, BSW27) near the camera. If a reduction of the specular reflection is desired, polarizers can be introduced into the optical paths, and the same mechanism can also be used to introduce other filters.

Mechanically, the air side and vacuum side of the microscope are two independent assemblies. A custom-made vacuum feedthrough allows the user to maintain precise mechanical alignment of the optical axis of the air side and vacuum side sections.

The live image of the microscope is displayed on a computer screen and covers an area of $\sim 600 \times 600\,\mu m$ on the sample. A calibrated crosshair on the screen allows targeting of locations of interest within the sample.

4. Microscope Performance

We tested the resolution of the microscope using a U.S. Air Force 1951 standard test target. It contains several groups of horizontal and vertical lines with decreasing width up to 228 lines/mm, which corresponds to a line width of 2.19 μm. Figure 3 shows that these features are well resolved, even though some chromatic aberration is present. However, this resolution was found to be sufficient to resolve targets of interest and ablation craters, both at micrometer dimensions. We have not observed any degradation of the optical performance due to the high vacuum even when pressures $<10^{-8}$ mbar are achieved.

For sampling microscopic features of interest, the translation vector V_{tr} (Fig. 1) between the laser focus and the microscope optical axis needs to be determined with high precision and reproducibility. V_{tr} was determined by shooting a crater into the sample surface and subsequent displacement of this crater into the center of the microscope image. One can then directly determine the V_{tr} from the stage coordinates. The reproducibility was assessed by moving the sample back by $-V_{tr}$ and generating a second crater on the same coordinates (Fig. 4). This was repeated 10 times, and a mean distance between the craters from the first and the second shot campaign of 2.7 μm with a standard deviation of $\sigma = 1.2\,\mu m$ was determined. This is well below the mean crater diameter of 14.1 ($\sigma = 2.1$) μm and guarantees a sufficient overlap of the coordinates after translation to the microscope and back. This calibration method was found to work reliably during the subsequent measurement campaigns.

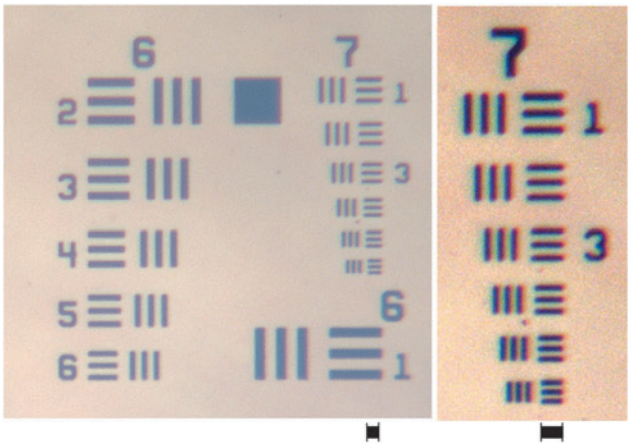

FIG. 3. Detail of the U.S. Air Force 1951 resolution test target recorded with the microscope system (left panel: real contrast; right panel: corrected contrast). The smallest line grid has a spacing of 2.19 μm and can be clearly resolved.

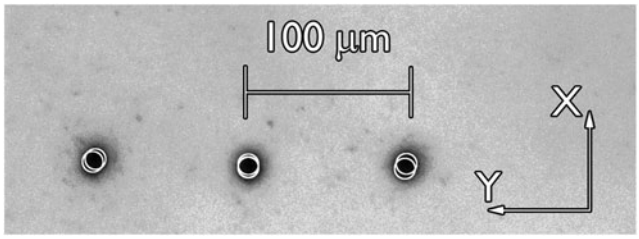

FIG. 4. Repeatability test of the translation from the mass spectrometer to the microscope in X and Y.

5. Mass Spectrometric Analysis of 1.9 Ga Old Microfossils in the Gunflint Chert

The Gunflint chert is an excellent case study for the combined use of the microscope and the mass spectrometer to detect traces of ancient life. The chert contains 1.9 Ga old micrometer-sized carbonaceous fossils in a dominantly SiO_2 matrix at different depth locations. The microfossils were described in detail in a series of articles in the 1960s and 1970s (Barghoorn and Tyler, 1965; Awramik and Barghoorn, 1977; Knoll *et al.*, 1978) and more recently have been studied and catalogued in terms of morphology, chemistry, and crystallography using modern techniques, including secondary ion mass spectrometry, focused ion beam, laser Raman, transmission electron microscopy, and scanning transmission X-ray microscopy (Moreau and Sharp, 2004; Wacey *et al.*, 2012, 2013; Alleon *et al.*, 2016; Lepot *et al.*, 2017). Our case study sample comes from the classic Schreiber Channel locality of the Gunflint chert on the north shore of Lake Superior (Wacey *et al.*, 2013). The Gunflint chert has also been suggested as an effective analogue to extraterrestrial rock formations that may contain microfossils (Brasier and Wacey, 2012). Thus, it is well suited to test and validate our recently improved measurement techniques and protocols for *in situ* detection of microfossils with our LIMS system.

For *in situ* detection of markers of present and past life, an elemental and isotopic mass spectrometric analysis at their precise location is required. In addition, sampling of the matrix as a reference in the vicinity, but not within a microfossil, is highly desirable (Brasier and Wacey, 2012). Sampling of the silica matrix is a challenging task for our LIMS system, because the sample matrix is nearly transparent at the wavelength of our IR laser (775 nm). Therefore, higher laser fluences of $\sim 10\,TW/cm^2$ are required, whereas good spectral quality and protection of the sample from excessive damage tend to drive the laser fluence down. Thanks to the direct optical feedback provided by the microscope, we were able to find optimal laser ablation parameters and sample the material with high spatial precision and sufficient spectral quality for elemental analysis.

Before sampling with the laser, the area of interest was mapped with the microscope. The map, composed of individual

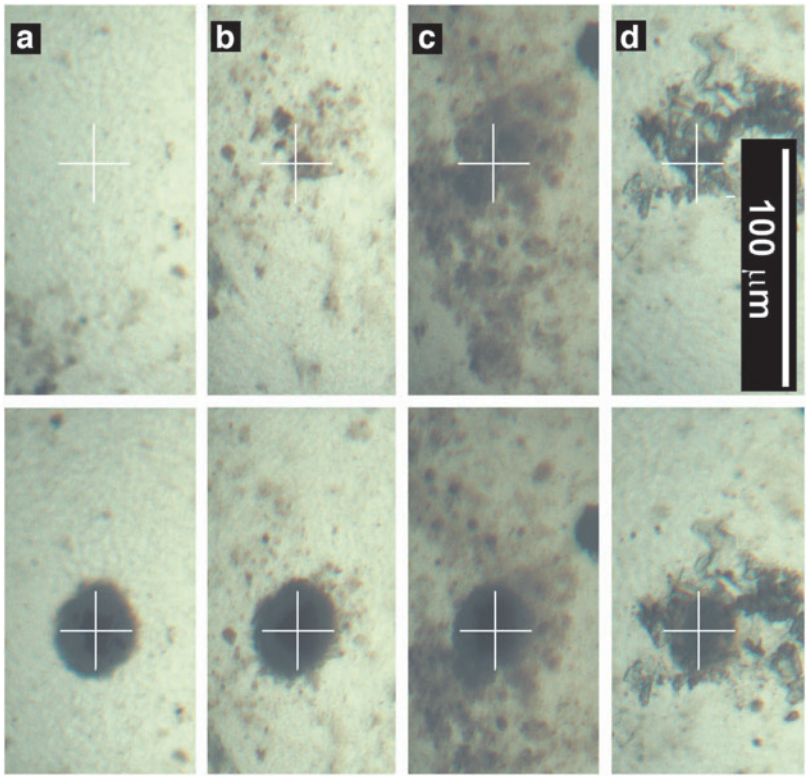

FIG. 5. Microscope picture of the colonies of microorganisms before and after sampling. The ablation craters as well as the surrounding affected zone are clearly visible. The scale is valid for all panels. Spots a, b, and c were sampled with 300,000 laser shots, d was sampled with 100,000 shots.

pictures of three adjacent areas, is displayed in Figure 5a, b, and d. Figure 5c shows a spot similar to that shown in Figure 5b in terms of color and shape, but ~3 mm away. The crosshairs represent the locations that were selected for sampling. Spot a is located in the silica matrix; the brown features at spots b to d are the clusters of small spheroidal, star-shaped, and filamentous fossils reported in many previous studies (*e.g.*, Barghoorn and Tyler, 1965; Knoll *et al.*, 1978; Lepot *et al.*, 2017). With the installed microscope, we can directly sample all these features with high position accuracy, since it provides the necessary *in situ* imaging capabilities and the possibility to control and possibly correct instrument and laser parameter settings. After sampling, the area was mapped again with the microscope to verify the ablation crater position and quality (Fig. 5, lower panels).

6. Results and Discussion

Figure 5, lower panels, shows the ablation craters and confirms that the desired features were successfully sampled. All craters show two distinct regions: a very dark inner area, which represents the actual crater (ø10–15 µm), and an outer rim with slightly lighter color (ø20–25 µm) called the ''affected zone.'' Detailed studies of the crater formation process were recently published by our group (Cedeño López *et al.*, 2018; Grimaudo *et al.*, 2018) and show that the sampled material actually originates only from the central crater region. The affected zone around the crater originates from redeposited material and altered surface properties due to the laser irradiation (*e.g.*, weak wings of laser radiation).

The mass spectra were analyzed using our in-house developed analysis software (Meyer *et al.*, 2017), and no relative sensitivity coefficients were applied to the measured element abundances. We observed that the signal-to-noise ratio (SNR) of the acquired signals is sufficient for the identification of many elements and isotopes of major elements. Despite the high laser fluence, the SNR of the recorded spectra was not sufficient to perform accurate isotopic analysis. In fact, many of the minor isotopes are still below the detection limit. Thus, an improvement of the SNR is desirable for future campaigns to perform isotopic analysis.

6.1. Spot a (300,000 laser shots, 10 TW/cm^2)

Figure 6 shows the mass spectra that were recorded at locations shown in Figure 5. The reference spectrum from the matrix acquired at location a shows dominant $^{28}Si^+$ and $^{16}O^+$ peaks. Also, the SiO^+ cluster is clearly present at m/q 44–46 as well as the Si_2^+ at m/q 56–58. Larger Si and O compounds can be found at m/q 60 (SiO_2^+), 72 (Si_2O^+), and 88 ($Si_2O_2^+$). $^{23}Na^+$, $^{27}Al^+$, $^{39}K^+$, and $^{41}K^+$, as well as $^{40}Ca^+$ can also readily be identified in the mass spectrum, along with low levels of $^{12}C^+$. Also at m/q 32 a peak can be observed. Although S may be present in the matrix in small quantities, both as micropyrite grains (Petrash *et al.*, 2016; Lepot *et al.*, 2017) and within finely disseminated organic material (Moreau and Sharp, 2004; Alleon *et al.*, 2016), it cannot be conclusively determined whether this peak originates from $^{32}S^+$, O_2^+, or a combination of both. To resolve this issue, an improvement of the SNR is required in further measurements, to raise the intensity of the corresponding ^{34}S peak above the detection limit, which would allow us to confirm or exclude the presence of S. At present, attributing the m/q 32 peak in this matrix spectrum to O_2^+ is the most likely explanation.

If we assume this spectrum to be a background mineral spectrum, an explanation must then be sought for those

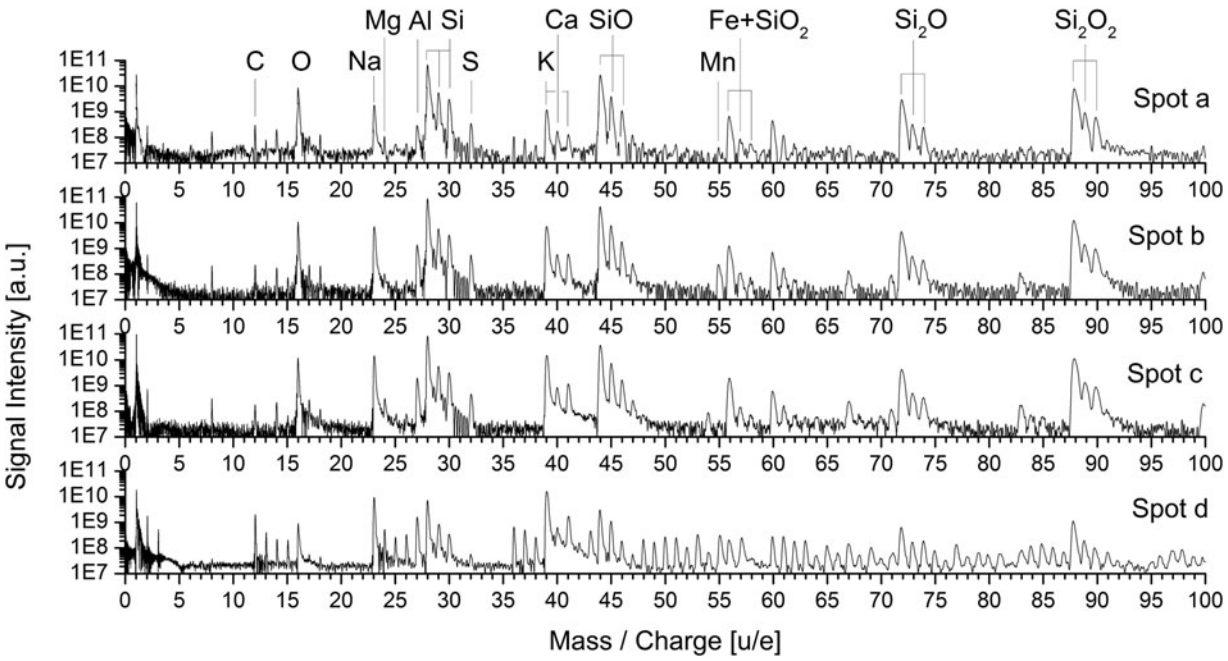

FIG. 6. Accumulated mass spectra from the four spots shown in Figure 5.

elements that are present in the spectrum but do not occur in the known dominant SiO_2 quartz matrix mineral phase. Na and K can have a number of sources; they are present in significant quantities in seawater, so may be incorporated into mineral salts (*e.g.*, chlorides and sulfates) as seawater evaporates in restricted environments. It is notable that silicified casts of cubic minerals interpreted as hopper halite (NaCl) have been reported from stromatolitic Gunflint samples (Petrash *et al.*, 2016), so the Na may be a remnant signal from these halite crystals. Na and K may also be incorporated into authigenic clay minerals or be brought into the system as detrital silicate minerals (*e.g.*, feldspars and clays). Little detrital input has previously been reported in these samples, but there have been reports of small volumes of (presumably authigenic) stilpnomelane in fossiliferous Gunflint samples (Schelble *et al.*, 2004), which would be a logical source for both the K and Al signals in our matrix spectrum.

The presence of Ca could also be explained by incorporation into evaporite minerals such as calcium sulfate (gypsum) or some types of aluminosilicate clay minerals, but such minerals have yet to be reported from fossiliferous members of the Gunflint Formation. Instead, a more logical explanation is that the Ca is contained within a carbonate mineral. A number of calcium-rich carbonates including calcite, dolomite, and ankerite have been reported from Gunflint sediments (Sommers *et al.*, 2000; Moreau and Sharp, 2004; Shapiro and Konhauser, 2015; Alleon *et al.*, 2016; Petrash *et al.*, 2016; Lepot *et al.*, 2017), and aragonite has been inferred to be the primary mineralizing phase of Gunflint stromatolites (Petrash *et al.*, 2016). Although much of this carbonate has subsequently been replaced by silica, large rhombic carbonate crystals still persist (Petrash *et al.*, 2016), and nanocarbonates are found sporadically within the silica matrix (*e.g.*, Lepot *et al.*, 2017). Hence, small volumes of calcite may explain both the Ca and small carbon signal from spot a. Alternatively, the carbon signal could arise from organic material dispersed in the matrix. We suggest this is less likely based on the optical images showing a clean mineral matrix at spot a.

6.2. Spot b (300,000 laser shots, 10 TW/cm^2)

On the microorganisms at spot b, the differences to the reference spectra found from spot a are rather subtle. One of the most striking differences is the presence of a peak at m/q = 55 (the Mn peak). Mn has previously been detected in a trace element study of stromatolites from the Schreiber Channel locality (Petrash *et al.*, 2016), and ankerite (a Mn-containing carbonate) rhombs are relatively common across Gunflint sediments (*e.g.*, Alleon *et al.*, 2016), so Mn was clearly present within Gunflint waters. Mn has been suggested as a possible metabolite for some of the star-shaped microorganisms preserved in the Gunflint chert (Cloud, 1965; John and Nudds, 2008). Thus, the detection of Mn may support the presence of a fossilized microbial community on this spot. The same microorganisms, plus some filamentous Gunflint forms, have also been suggested to oxidize Fe (Planavsky *et al.*, 2009) although other authors have a different view (Shapiro and Konhauser, 2015). Hence, this element might be expected to be found at the same location. Unfortunately, in the current measurement, the main $^{56}Fe^+$ peak overlaps with the Si_2^+ cluster, and the signal of $^{54}Fe^+$ is not strong enough to be detected above the background. However, by comparing the signal intensities between the peaks at m/q = 28 ($^{28}Si^+$) and 56($^{28}Si_s^+ + {}^{56}Fe^+$), we can infer the presence of Fe.

Table 1 presents the ratios between the peaks at m/q = 56 and 28 (third column). The peak intensity ratio is 10.6×10^{-3} and 19.32×10^{-3} for spots a and b, respectively, which indicates a clear enhancement of the signal at spot b. This supports the enrichment of Fe in position b. To verify that the enhancement actually originates from a $^{28}Si_2^+/^{56}Fe^+$ isobar and not from a random change in instrument or measurement

Table 1. Peak Ratios for the 56 Isobar, Plus Single and Double Charged Species as a Reference to Verify Unchanged Instrument Conditions and Ion Formation

Ratio Spot	$^{28}Si^{2+}/{}^{28}Si^{+}\times10^{-3}$	$(^{28}Si_2^{+}+{}^{56}Fe^{+})/{}^{28}Si^{+}\times10^{-3}$	$^{60}(SiO_2)^{+}/{}^{28}Si^{+}\times10^{-3}$
a	3.1 ± 0.2	10.6 ± 0.1	3.5 ± 0.2
b	3.40 ± 0.01	19.32 ± 0.02	4.08 ± 0.02
b/a	1.09 ± 0.07	1.82 ± 0.02	1.15 ± 0.07

Enhancement of the isobaric peak at m/q = 56 compared with the surrounding clusters confirms the presence of Fe at location b.

parameters, we also investigated surrounding peaks that should not be affected by the presence of iron. We chose the Si^{2+} and the SiO_2^{+} peak at m/q = 14 and 60, respectively, as a reference, since they do not interfere with a Fe or Fe-cluster peak and are only dependent on highly abundant elements of the matrix. The results are listed in the second and fourth columns, respectively, of Table 1.

Within error bars the reference peak intensities stay constant between spots a and b, indicating that the laser ablation took place at very similar conditions on both spots. Thus, it can be concluded that this enhancement of the 56 peak at spot b is really due to the contribution of Fe.

Compared with the reference on the matrix spot a, the abundance of ^{40}Ca is enhanced by a factor of 5, supporting the increased presence of Ca carbonates at spot b. However, the interference by the neighboring peaks renders the measurement of the abundance less certain. Also, the second most important isotope ^{44}Ca cannot be measured because of the interference with the SiO^{+} cluster. Nonetheless, an increased abundance of Ca associated with the organics of spot b would be consistent with previous observations of nanoscale mixing of cellular organic material and carbonates in the Gunflint Formation (Alleon *et al.*, 2016).

The peak at m/q = 24 suggests the presence of Mg on this spot that would be consistent with a dolomitic composition for the aforementioned carbonate (cf. Petrash *et al.*, 2016), but since C is also present in the spectrum, it could also result from a C_2^{+} cluster. The C content at this spot is rather low, so that the formation of C_x and C_xH_y clusters appears to be a less likely interpretation of this peak. Unfortunately, the SNR of this peak is insufficient to be detected by the peak-finding algorithm (Meyer *et al.*, 2017) and no abundance could be determined for this peak (hence it is missing in Fig. 7).

We further observed an enhancement of the ^{27}Al abundance on the potential cluster of fossils by a factor of 18, accompanied by significant increases in the $^{23}Na^{+}$, $^{39}K^{+}$, and $^{41}K^{+}$ peaks, suggesting an elevated presence of aluminosilicates. This is consistent with data from other Precambrian microfossil sites where organisms can be partially permineralized by aluminosilicates (Wacey *et al.*, 2014), with evidence from modern settings showing that biofilms may trap detrital clay minerals on their ''sticky'' extracellular polymeric substances (Riding, 2000) and with evidence for aluminosilicates associated with other Gunflint microfossils (Schelble *et al.*, 2004)

6.3. Spot c (300,000 laser shots, 10 TW/cm^2)

The microscope pictures of spots b and c are very similar in terms of color and shapes. The main difference between the two microbial colonies is their size and density. The

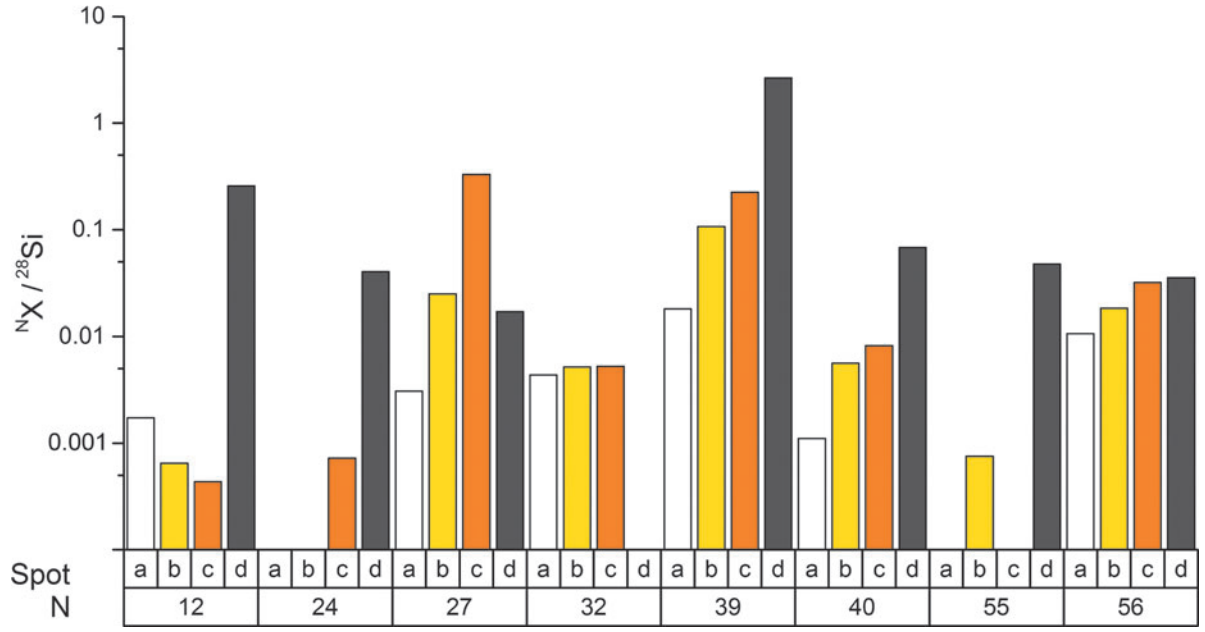

FIG. 7. Relative abundances of selected isotopes and clusters $^{12}C^{+}$, $^{24}Mg^{+}$, $^{27}Al^{+}$, $^{32}S^{+}/O_2^{+}$, $^{39}K^{+}$, $^{40}Ca^{+}$, $^{55}Mn^{+}$, and $^{56}(Fe^{+} + Si_2^{+})$ on the four sampled spots shown in Figure 5. Missing bars mean that the peak integration failed due to insufficient signal-to-noise ratio. The $^{32}S^{+}/O_2^{+}$ abundance is similar for the measured spots a, b, and c. The measured abundance of K, Ca, and Fe correlates for spots b and c, suggesting that similar types of microorganisms were present on both spots, but with a larger population on spot c. This is supported by the microscope images. The chemical analysis of d shows a rather different composition to the other spots, which is also supported by the microscope pictures.

colony at spot c is >100 μm long, whereas the colony at spot c is only 10–20 μm in length.

The comparison of the mass spectra (Figs. 6 and 7) shows that they are also chemically similar, although not the same. The peak at m/q = 24 is more intense at spot c. This could suggest a higher Mg abundance, presumably from a Ca–Mg carbonate (dolomite) mineral on this spot. However, a contribution from the C_2^+ cluster seems a more plausible explanation for spot b, since a series of potential $C_xH_y^+$ clusters are also visible in the higher mass range.

The Al/Si ratio is enhanced by a factor of 107 compared with the reference spot a, again consistent with an association of aluminosilicates (probably clay minerals) with microfossils (cf. Wacey *et al.*, 2014). The peak at m/q = 54 can be attributed to a $^{54}Al_2^+$ cluster. A stronger Fe contribution and the presence of $^{54}Fe^+$ are unlikely since the intensities for the $^{56}Fe^+$ peaks are comparable with those of spots a and b. The $^{55}Mn^+$ peak observed at location b is completely absent on this spot, suggesting that only spheroidal and filamentous microorganisms, not the putative Mn-metabolizing star-shaped organisms (cf. Cloud, 1965), are present here.

6.4. Spot d (100,000 laser shots, 10 TW/cm^2)

The cluster of microorganisms on spot d has a chemical composition that is significantly different to the reference spot a and subtly different to the microorganism clusters at spots b and c. The measured Na and K abundances are almost as large as the O abundance, and ^{12}C is very abundant. The high abundance of carbon leads to the formation of the typical C_x and C_xH_y series of clusters at m/q = 24 (Tulej *et al.*, 2015). For this reason, it is not possible to clearly identify minor elements in some parts of the mass spectrum on this spot. However, we do once again note the presence of $^{55}Mn^+$, and this signal is more intense than at spot b, plus elevated Al, Ca, and Fe (summarized in Fig. 7). Elevated Na, K, Mn, Al, Ca, and Fe are all consistent with the intimate association of organic material with nanograins of carbonates and clay minerals as previously observed with fossiliferous domains of the Gunflint chert (Alleon *et al.*, 2016; Lepot *et al.*, 2017). Of course, the high ^{12}C signal, plus the presence of C_x and C_xH_y clusters, provides by far the strongest evidence for the detection of microbial fossils at this spot, since ^{12}C is not only commonly preserved within ancient fossilized cell walls (Wacey *et al.*, 2012; Lepot *et al.*, 2017) but can also be retained in fossilized extracellular envelopes (Wacey *et al.*, 2010).

7. Conclusion

In this article we introduce the design of our high vacuum compatible microscope combined with our miniature LIMS system, and its significance for the optical and chemical detection of fossils at micrometer dimensions. We discuss its performance, including the resolving power of 1 μm, and its capability to map samples and acquire mass spectra with a spatial precision of ~2 μm. The method of targeting samples at precisely defined locations maximizes the scientific output of the measurement campaign. Compared with the traditional rastering method, it also represents a vast increase in measuring efficiency since only regions of interest are sampled. Using the Gunflint chert, serving as a potential Mars analog sample we showed the importance of a system combining mass spectrometry and microscopy for the *in situ* analysis of fossilized microbes.

We distinguished and sampled four different regions of interest on the Gunflint chert and found a number of potential indicators for the presence of the fossilized microorganisms, based on comparisons of these spectra. These included elevated levels of carbon plus C_x and C_xH_y clusters, together with elevated levels of elements that the microorganisms could have metabolized (*e.g.*, Mn and Fe). A number of other elements showed higher concentrations in the vicinity of clusters of microbes, but further work is required to understand whether these were concentrated by biological activity or merely passively accumulated in these regions. However, a tentative assignment of the regions to different types of microorganisms including filamentous, spheroidal, and star-shaped specimens was performed.

Acknowledgments

This work is supported by the Swiss National Science Foundation. D.W. is supported by an Australian Research Council Future Fellowship (FT140100321). Prof. Dr. Herbert Shea from EPFL/LMTS is thanked for his support.

Author Disclosure Statement

No competing financial interests exist.

References

Alleon, J., Bernard, S., Le Guillou, C., Marin-Carbonne, J., Pont, S., Beyssac, O., McKeegan, K.D., and Robert, F. (2016) Molecular preservation of 1.88 Ga Gunflint organic microfossils as a function of temperature and mineralogy. *Nat Commun* 7:11977.

Awramik, S.M. and Barghoorn, E.S. (1977) Gunflint microbiota. *Precambrian Res* 5:121–142.

Barghoorn, E.S. and Tyler, S.A. (1965) Microorganisms from the Gunflint Chert: these structurally preserved Precambrian fossils from Ontario are the most ancient organisms known. *Science* 147:563–575.

Beard, B.L., Johnson, C.M., Cox, L., Sun, H., Nealson, K.H., and Aguilar, C. (1999) Iron isotope biosignatures. *Science* 285: 1889–1892.

Brasier, M.D. and Wacey, D. (2012) Fossils and astrobiology: new protocols for cell evolution in deep time. *Int J Astrobiol* 11:217–228.

Brinckerhoff, W.B., Managadze, G.G., McEntire, R.W., Cheng, A.F., and Green, W.J. (2000) Laser time-of-flight mass spectrometry for space. *Rev Sci Instrum* 71:536–545.

Cameron, V., Vance, D., Archer, C., and House, C.H. (2009) A biomarker based on the stable isotopes of nickel. *Proc Natl Acad Sci U S A* 106:10944–10948.

Cedeño López, A., Grimaudo, V., Moreno-García, P., Riedo, A., Tulej, M., Wiesendanger, R., Wurz, P., and Broekmann, P. (2018) Towards femtosecond laser ablation ionization mass spectrometric approaches for chemical depth-profiling analysis of lead-free Sn solder bumps with minimized sidewall contributions. *J Anal Atom Spectrom* 33:283–293.

Chela-Flores, J. and Kumar, N. (2008) Returning to Europa: can traces of surficial life be detected? *Int J Astrobiol* 7:263–269.

Chela-Flores, J. and Seckbach, J. (2011) The Dry Valley Lakes, Antarctica: from sulfur stains on Earth to sulfur stains in the Jovian system. In: *Proceedings of the SPIE, Instruments, Methods, and Missions for Astrobiology Xiv*, pp. 81520R-81520R-8, DOI: 10.1117/12.898763.

Chela-Flores, J., Cicuttin, A., Crespo, M. L., and Tuniz, C. (2015) Biogeochemical fingerprints of life: earlier analogies with polar ecosystems suggest feasible instrumentation for probing the Galilean moons. *Int J Astrobiol* 14:427–434.

Cloud, P.E. (1965) Significance of Gunflint (Precambrian) microflora—photosynthetic oxygen may have had important local effects before becoming a major atmospheric gas. *Science* 148:27.

Cui, Y., Moore, J.F., Milasinovic, S., Liu, Y.M., Gordon, R.J., and Hanley, L. (2012) Depth profiling and imaging capabilities of an ultrashort pulse laser ablation time of flight mass spectrometer. *Rev Sci Instrum* 83.

Grimaudo, V., Moreno-Garcia, P., Riedo, A., Neuland, M.B., Tulej, M., Broekmann, P., and Wurz, P. (2015) High-resolution chemical depth profiling of solid material using a miniature laser ablation/ionization mass spectrometer. *Anal Chem* 87:2037–2041.

Grimaudo, V., Moreno-Garcia, P., Riedo, A., Meyer, S., Tulej, M., Neuland, M.B., Mohos, M., Gutz, C., Waldvogek, S.R., Wurz, P., and Broekmann, P. (2017) Toward three-dimensional chemical imaging of ternary Cu-Sn-Pb alloys using femtosecond laser ablation/ionization mass spectrometry. *Anal Chem* 89:1632–1641.

Grimaudo, V., Moreno-García, P., Cedeño López, A., Riedo, A., Wiesendanger, R., Tulej, M., Gruber, C., Lörtscher, E., Wurz, P., and Broekmann, P. (2018) Combining anisotropic etching and PDMS casting for three-dimensional analysis of laser ablation process. *Anal Chem* 90:2692–2700.

Guest, W.H. (1984) Recent developments of laser microprobe mass analyzers, Lamma-500 and Lamma-1000. *Int J Mass Spectrom Ion Process* 60:189–199.

Hanauske, U., Hanauske, A.R., Marshall, M.H., Muggia, V.A., and Von Hoff, D.D. (1987) Biphasic effect of vanadium salts on in vitro tumor colony growth. *Int J Cell Cloning* 5:170–178.

Heinen, H.J., Meier, S., Vogt, H., and Wechsung, R. (1983) Lamma-1000, a new laser microprobe mass analyzer for bulk samples. *Int J Mass Spectrom Ion Process* 47:19–22.

Hofmann, B.A. (2008) Morphological biosignatures from subsurface environments: recognition on planetary missions. *Space Sci Rev* 135:245–254.

Hornung, K., Kissel, J., Fischer, H., Mellado, E.M., Kulikov, O., Hilchenbach, M., Kruger, H., Engrand, C., Langevin, Y., Rossi, M., and Krueger, F.R. (2014) Collecting cometary dust particles on metal blacks with the COSIMA instrument onboard ROSETTA. *Planet Space Sci* 103:309–317.

Huang, R.F., Lin, Y.M., Li, L.F., Hang, W., He, J., and Huang, B.L. (2010) Two-dimensional separation in laser ionization orthogonal time-of-flight mass spectrometry. *Anal Chem* 82: 3077–3080.

John, R. and Nudds, P.A.S. (2008) *Fossil Ecosystems of North America: A Guide to the Sites and Their Extraordinary Biotas*, Manson Publishing Ltd., London, United Kingdom.

Knoll, A.H., Barghoorn, E.S., and Awramik, S.M. (1978) New microorganisms from Aphebian Gunflint Iron Formation, Ontario. *J Paleontol* 52:976–992.

Kuznetsov, I., Filevich, J., Dong, F., Woolston, M., Chao, W.L., Anderson, E.H., Bernstein, E.R., Crick, D.C., Rocca, J.J., and Menoni, C.S. (2015) Three-dimensional nanoscale molecular imaging by extreme ultraviolet laser ablation mass spectrometry. *Nat Commun* 6.

Lepot, K., Addad, A., Knoll, A.H., Wang, J., Troadec, D., Beche, A., and Javaux, E.J. (2017) Iron minerals within specific microfossil morphospecies of the 1.88 Ga Gunflint formation. *Nat Commun* 8.

Ma, Z., Thompson, R.N., Lykke, K.R., Pellin, M.J., and Davis, A.M. (1995) New instrument for microbeam analysis incorporating submicron imaging and resonance ionization mass-spectrometry. *Rev Sci Instrum* 66:3168–3176.

Managadze *et al*. (2017) A new method and mass-spectrometric instrument for extraterrestrial life detection using the elemental composition analyses of Martian Regolith and Permafrost/Ice. *Astrobiology* 17:448–458.

Marshall, C.P., Olcott Marshall, A., Aitken, J.B., Lai, B., Vogt, S., Breuer, P., Steemans, P., and Lay, P.A. (2017) Imaging of vanadium in microfossils: a new potential biosignature. *Astrobiology* 17:1069–1076.

Meyer, S., Riedo, A., Neuland, M.B., Tulej, M., and Wurz, P. (2017) Fully automatic and precise data analysis developed for time-of-flight mass spectrometry. *J Mass Spectrom* 52:580–590.

Monster, J., Appel, P.W.U., Thode, H.G., Schidlowski, M., Carmichael, C.M., and Bridgwater, D. (1979) Sulfur isotope studies in early Archaean sediments from Isua, West Greenland—implications for the antiquity of bacterial sulfate reduction. *Geochim Cosmochim Acta* 43:405–413.

Moreau, J.W. and Sharp, T.G. (2004) A transmission electron microscopy study of silica and kerogen biosignatures in-1.9 Ga gunflint microfossils. *Astrobiology* 4:196–210.

Moreno-Garcia, P., Grimaudo, V., Riedo, A., Tulej, M., Neuland, M.B., Wurz, P., and Broekmann, P. (2016) Towards structural analysis of polymeric contaminants in electrodeposited Cu films. *Electrochim Acta* 199:394–402.

Neuland, M.B., Meyer, S., Mezger, K., Riedo, A., Tulej, M., and Wurz, P. (2014) Probing the Allende meteorite with a miniature laser-ablation mass analyser for space application. *Planet Space Sci* 101:196–209.

Ohmoto, H., Kakegawa, T., and Lowe, D.R. (1993) 3.4-Billion-year-old biogenic pyrites from Barberton, South-Africa—sulfur isotope evidence. *Science* 262:555–557.

Ono, S. (2008) Multiple-sulphur isotope biosignatures. *Space Sci Rev* 135:203–220.

Petrash, D.A., Robbins, L.J., Shapiro, R.S., Mojzsis, S.J., and Konhauser, K.O. (2016) Chemical and textural overprinting of ancient stromatolites: timing, processes, and implications for their use as paleoenvironmental proxies. *Precambrian Res* 278:145–160.

Planavsky, N., Rouxel, O., Bekker, A., Shapiro, R., Fralick, P., and Knudsen, A. (2009) Iron-oxidizing microbial ecosystems thrived in late Paleoproterozoic redox-stratified oceans. *Earth Planet Sci Lett* 286:230–242.

Redfield, A.C. (1934) James Johnstone memorial volume. University Press of Liverpool, Liverpool.

Riding, R. (2000) Microbial carbonates: the geological record of calcified bacterial-algal mats and biofilms. *Sedimentology* 47:179–214.

Riedo, A., Bieler, A., Neuland, M., Tulej, M., and Wurz, P. (2013a) Performance evaluation of a miniature laser ablation time-of-flight mass spectrometer designed for in situ investigations in planetary space research. *J Mass Spectrom* 48:1–15.

Riedo, A., Meyer, S., Heredia, B., Neuland, M.B., Bieler, A., Tulej, M., Leya, I., Iakovleva, M., Mezger, K., and Wurz, P. (2013b) Highly accurate isotope composition measurements by a miniature laser ablation mass spectrometer designed for in situ investigations on planetary surfaces. *Planet Space Sci* 87:1–13.

Riedo, A., Neuland, M., Meyer, S., Tulej, M., and Wurz, P. (2013c) Coupling of LMS with a fs-laser ablation ion source: elemental and isotope composition measurements. *J Anal At Spectrom* 28:1256–1269.

Riedo, A., Grimaudo, V., Moreno-Garcia, P., Neuland, M.B., Tulej, M., Wurz, P., and Broekmann, P. (2015) High depth-resolution laser ablation chemical analysis of additive-assisted Cu electroplating for microchip architectures. *J Anal At Spectrom* 30:2371–2374.

Riedo, A., Tulej, M., Rohner, U., and Wurz, P. (2017) High-speed microstrip multi-anode multichannel plate detector system. *Rev Sci Instrum* 88:045114.

Rohner, U., Whitby, J. A., and Wurz, P. (2003) A miniature laser ablation time-of-flight mass spectrometer for in situ planetary exploration. *Meas Sci Technol* 14:2159–2164.

Schelble, R.T., Westall, F., and Allen, C.C. (2004) similar to 1.8 Ga iron-mineralized microblota from the Gunflint Iron Formation, Ontario, Canada: implications for Mars. *Space Life Sci* 33:1268–1273.

Shapiro, R.S. and Konhauser, K.O. (2015) Hematite-coated microfossils: primary ecological fingerprint or taphonomic oddity of the Paleoproterozoic? *Geobiology* 13:209–224.

Shen, Y.A., Buick, R., and Canfield, D.E. (2001) Isotopic evidence for microbial sulphate reduction in the early Archaean era. *Nature* 410:77–81.

Sommers, M.G., Awramik, S.M., and Woo, K.S. (2000) Evidence for initial calcite-aragonite composition of Lower Algal Chert Member ooids and stromatolites, Paleoproterozoic Gunflint Formation, Ontario, Canada. *Can J Earth Sci* 37: 1229–1234.

Summons, R.E., Amend, J.P., Bish, D., Buick, R., Cody, G.D., Des Marais, D.J., Dromart, G., Eigenbrode, J.L., Knoll, A.H., and Sumner, D.Y. (2011) Preservation of martian organic and environmental records: final report of the Mars Biosignature Working Group. *Astrobiology* 11:157–181.

Thomas, N., Luthi, B.S., Hviid, S.F., Keller, H.U., Markiewcz, W.J., Blumchen, T., Basilevsky, A.T., Smith, P.H., Tanner, R., Oquest, C., Reynolds, R., Josset, J.L., Beauvivre, S., Hofmann, B., Rüffer, P., and Pillinger, C.T. (2004) The microscope for Beagle 2. *Planet Space Sci* 52:853–866.

Tulej, M., Riedo, A., Neuland, M.B., Meyer, S., Wurz, P., Thomas, N., Grimaudo, V., Moreno-Garcia, P., Broekmann, P., Neubeck, A., and Ivarsson, M. (2014) CAMAM: a Miniature laser ablation ionisation mass spectrometer and microscope-camera system for in situ investigation of the composition and morphology of extraterrestrial materials. *Geostand Geoanal Res* 38:441–466.

Tulej, M., Neubeck, A., Ivarsson, M., Riedo, A., Neuland, M.B., Meyer, S., and Wurz, P. (2015) Chemical composition of micrometer-sized filaments in an aragonite host by a miniature laser ablation/ionization mass spectrometer. *Astrobiology* 15:669–682.

Vago, J.L., Westall, F., Coates, A.J., Jaumann, R., Korablev, O., Ciarletti, V., Mitrofanov, I., Josset, J.L., De Sanctis, M.C., Bibring, J.P., Rull, F., Goesmann, F., Steininger, H., Goetz, W., Brinckerhoff, W.B., Szopa, C., Raulin, F., Edwards, H.G.M., Whyte, L.G., Fairén, A.G., Bridges, J.F.P., Hauber, E., Ori, G.G., Werner, S.L., Loizeau, D., Kuzmin, R.O., Williams, R., Flahaut, J., Forget, F., Rodionov, D.S., Svedhem, H., Sefton-Nash, E., Kminek, G., Lorenzoni, L., Joudrier, L., Mikhailov, V., Zashchirinskiy, A., Alexashkin, S., Calantropio, F., Merlo, A., Poulakis, P., Witasse, O., Bayle, O., Bayón, S., Meierhenrich, U.J., Carter, J., García-Ruíz, J.M., Baglioni, P., Haldemann, A.F.C., Ball, A.J.S., André Debus, Lindner, R., Haessig, F., Monteiro, D., Trautner, R., Voland, C., Rebeyre, P., Goulty, D., Didot, F., Durrant, S., Zekri, E., Koschny, D., Toni, A., Visentin, G., Zwick, M., M. van Winnendael, Azkarate, M., and Carreau, C. (2017) Habitability on early mars and the search for biosignatures with the ExoMars rover. *Astrobiology* 17:471–510.

Wacey, D., Gleeson, D., and Kilburn, M.R. (2010) Microbialite taphonomy and biogenicity: new insights from NanoSIMS. *Geobiology* 8:403–416.

Wacey, D., Kilburn, M.R., Saunders, M., Cliff, J., and Brasier, M.D. (2011) Microfossils of sulphur-metabolizing cells in 3.4-billion-year-old rocks of Western Australia. *Nat Geosci* 4:698–702.

Wacey, D., Menon, S., Green, L., Gerstmann, D., Kong, C., Mcloughlin, N., Saunders, M., and Brasier, M. (2012) Taphonomy of very ancient microfossils from the similar to 3400 Ma Strelley Pool Formation and similar to 1900 Ma Gunflint Formation: new insights using a focused ion beam. *Precambrian Res* 220:234–250.

Wacey, D., McLoughlin, N., Kilburn, M.R., Saunders, M., Cliff, J.B., Kong, C., Barley, M.E., and Brasier, M.D. (2013) Nanoscale analysis of pyritized microfossils reveals differential heterotrophic consumption in the ~1.9-Ga Gunflint chert. *Proc Natl Acad Sci U S A* 110:8020–8024.

Wacey, D., Saunders, M., Roberts, M., Menon, S., Green, L., Kong, C., Culwick, T., Strother, P., and Brasier, M.D. (2014) Enhanced cellular preservation by clay minerals in 1 billion-year-old lakes. *Sci Rep* 4:5841.

Westall, F., Nijman, W., Brack, A., Steele, A., and Toporski, J. (2001) The oldest fossil life on Earth, its geological context and life on Mars. In Proceedings of First European Workshop on Exo-/Astrobiology. Froscati (IT), pp. 81–90.

Wiesendanger, R., Tulej, M., Riedo, A., Frey, S., Shea, H., and Wurz, P. (2017) Improved detection sensitivity for heavy trace elements using a miniature laser ablation ionisation mass spectrometer. *J Anal At Spectrom*

Zhang, B.C., He, M.H., Hang, W., and Huang, B.L. (2013) Minimizing matrix effect by femtosecond laser ablation and ionization in elemental determination. *Anal Chem* 85:4507–4511.

Zonnevylle, A.C., Van Tol, R.F., Liv, N., Narvaez, A.C., Effting, A.P., Kruit, P., and Hoogenboom, J.P. (2013) Integration of a high-NA light microscope in a scanning electron microscope. *J Microsc* 252:58–70.

Address correspondence to:
Reto Wiesendanger
Space Research and Planetary Sciences
Physics Institute
University of Bern
Sidlerstrasse 5
Bern CH-3012
Switzerland

E-mail: reto.wiesendanger@space.unibe.ch

Submitted 27 October 2017
Accepted 7 March 2018

Abbreviations Used

DOF = depth of focus
LA-TOF-MS = laser ablation ionization time-of-flight mass spectrometer
LIMS = laser ablation ionization mass spectrometry
NA = numerical aperture
OP1 = optical path 1
OP2 = optical path 2
SNR = signal-to-noise ratio